

EXPERIMENTAL AND NUMERICAL CONFIGURATION STUDY ON UCAV'S AERODYNAMICS

X. Z. Huang, Y. Mébarki, and A. Benmeddour

Institute for Aerospace Research, National Research Council of Canada

Keywords: UCAV, high angle of attack, maneuverability, leading-edge vortex

Abstract

Configuration studies of future Unmanned Combat Air Vehicle (UCAV), such as leading-edge shape, centerbody and wing platform, were conducted both experimentally and numerically. More than 50 configurations were investigated. Aerodynamic loads, surface pressure, and flow visualization data were collected. The range of the angle of attack was from where the leading-edge vortex is fully developed up to where the leading-edge vortex is totally broken down. The Re_{mac} numbers are approximately 2×10^6 and 2×10^4 in wind tunnel and water tunnel respectively. The CFD solutions were obtained using a 3D unstructured grid Euler solver, FJ3SOLV, developed at IAR. It is a cell-centered code based on the finite volume formulation. Unstructured tetrahedral meshes of about 500,000 cells were generated using the Octree based Tetra module.

1 Nomenclature

a, b, c, d	coefficients used in Eqn. 1
c_0	root chord
C_m	Pitching moment coefficient
C_N	Normal force coefficient
mac	mean aerodynamic chord
s	local semi-span
U	free stream velocity (m/s)
x, y, z	body axes
x_n	distance normal to the leading-edge
x_{vb}	non dimensional vortex breakdown location, x/c_0
α	angle of attack ($^\circ$)
ϕ	roll angle ($^\circ$)
Λ	leading-edge sweep ($^\circ$)

2 Introduction

Future unmanned combat aerial vehicles (UCAVs) aim at high maneuverability and agility. In order to achieve these goals, two design features are notable: 1) the conventional forebody is replaced by a relatively small center body on the wing upper surface and 2) most of the UCAVs may adopt a planform of delta, double delta or diamond as its basic configuration shown in Fig. 1. Since the UCAVs usually operate at near- and post-stall regimes for extra aerodynamic lift and control power created by leading-edge vortices, the leading-edge shape and the planform will significantly affect the boundary layer separation and the behavior of the leading-edge vortex. In order to understand and further improve the behavior of UCAVs, the effects of geometrical changes, e.g. leading-edge shape, wing platform, and center body, on the aerodynamics of UCAVs have to be studied.

On the other hand, although the rapid progress in hardware and computational fluid dynamics (CFD) software has given the opportunity to numerically simulate aerodynamic flow phenomena like vortex flow and vortex breakdown, the solution is based on assumed separation lines and boundary layer transition lines. It is not possible at this stage to relax these assumptions and to handle the effects of leading-edge geometry on the separation and transition lines. Thus, to extending the CFD solutions to these areas and validate the solutions, will be an important step towards real UCAVs' applications.

To this end, experimental and computational studies were conducted.

In the experimental studies, both wind tunnel and water tunnel experiments were performed. More than 50 different configurations were tested in the wind tunnel and water tunnel. The wind tunnel models included a diamond wing with a 55° leading-edge sweep and two delta wings with leading edge sweeps of 55° and 65° . The wind tunnel models had different leading-edge shapes and center body settings. The water tunnel models consisted of delta wings with the leading edge sweep ranging from 55° to 75° . Pressure sensitive paint (PSP), pressure orifices, and balance measurements as well as flow visualization tests were conducted. The angle of attack ranged from the point where the leading-edge vortex was fully developed up to the point where the leading-edge vortex was fully broken down. The Reynolds numbers (based on mac) are approximately 2×10^6 and 2×10^4 in the wind tunnel and water tunnel, respectively.

The computational studies were performed on a 55° diamond wing and a 65° delta wing with sharp leading edges. To numerically assess the centerbody effects, with and without centerbody configurations of the two wings were computed. An in-house developed inviscid flow solver, FJ3SOLV, was used in the calculations. Being based on the solution of Euler equations, which are capable of predicting rotational flows, FJ3SOLV can capture the formation of vortices from sharp edges. In addition, numerical results obtained at the NASA LaRC for the 65° delta wing with centerbody are also included for comparison.

2 Experimental Approaches

2.1 Models

The more than 50 models configurations tested are catalogued into three groups (G1, G2 and G3).

The models in G1 (Fig. 2) consist of the diamond wing and the delta wing with the 55° leading edge sweep. Their leading-edge, center body and aft portion of the wing were

interchangeable. Thus, the model could be easily changed from diamond (sub-group G1-1, Fig. 2a) to delta wing with different leading-edge shapes, and with or without center body (subgroup G1-2, Fig. 2b, and subgroup G1-3, Fig. 2c). Five different leading-edge shapes were manufactured indicated by A, B, C, D and E in Fig. 2, i.e. a large-radius, a medium-radius and three sharp leading-edges (symmetric bevel, flat-up and flat-down). The sharp leading-edges had 40° of total bevel angle. While the rounded leading-edge shapes had leading-edge radii of 0.15% and 0.3% normalized by the mac of the delta wing (Model G1-2) for medium- and large-radius leading-edges respectively. The shapes for these rounded leading-edges were determined by the following equation:

$$z = ax_n^{0.5} + bx_n + cx_n^2 + dx_n^3 \quad (1)$$

where the coefficients a , b , c and d were taken as in the following table:

leading-edge	a	b	c	d
medium-radius	0.1972	0.2117	-0.3349	0.1199
large-radius	0.2697	0.0566	-0.2252	0.0863

The models in the second group (G2) were based on a 65° leading edge configuration, the same geometry as used in the IAR/USAF program. Thus, the previous edited comprehensive data [1] can be used in this study. However, the distinguishing feature of the current model is that it consisted of upper and lower wing halves made of PVC and stainless steel respectively (Fig. 3). The upper wing half (PVC wing half) had 57 pressure orifices. Some pressure orifices are located on the centerbody. The lower wing half, which supports the air loads acting on the wing, was made of stainless steel. The centerbody also consisted of an upper half and a lower half. Similar to the models in the first group, their leading-edge and centerbody were interchangeable (Fig. 3a). Therefore it had many combinations (Fig. 3b) such as sharp or rounded leading-edge, with or without centerbody, etc. The rounded leading-edge shapes had leading-edge radii of 0.15% and 0.3% respectively and

were determined using equation (1), but with different coefficients given in the table below:

leading-edge	<i>a</i>	<i>b</i>	<i>c</i>	<i>d</i>
medium-radius	0.255	-0.005	-0.1089	0.0472
large-radius	0.3897	-0.1682	-0.0753	0.0414

The coordinates of the 57 pressure orifices on the 65° wing upper (PVC) surface are given in the tables below:

<i>x</i>	<i>y/s</i>							
0.4	0.00	0.17	0.24	0.30	0.34	0.40	0.50	0.55
0.6(0.62)	0.00*	0.12	0.16	0.20	0.25	0.30	0.35	0.40
0.75	0.00	0.09	0.13	0.16	0.18	0.28	0.36	0.44

<i>x</i>	<i>y/s</i>							
0.4	0.60	0.70	0.80	0.90				
0.6	0.50	0.55	0.60	0.65	0.70	0.80	0.90	
0.75	0.52	0.60	0.64	0.68	0.72	0.76	0.84	0.92 -0.68

The locations of the first four rows are under the centerbody or under the fairing. Two sets of orifices were made at each location: one on the surface of the centerbody or the fairing and another on the PVC wing surface. Thus, either the pressure on the centerbody or on the wing surface (when the centerbody was taken away) could be measured. It should be pointed out that one of the main purposes of using the pressure orifices was to calibrate and to confirm the PSP results. After the trial test on the 65° delta wing, which showed good comparisons between PSP and pressure orifice measurements, in the later tests with the 55° diamond and delta wing models only three pressure orifices were used to check the PSP results.

The aerodynamic loads were measured by an 6-component balance mounted inside the lower part of the centerbody.

The tests were conducted in the IAR 2m x 3m Low Speed Wind Tunnel at free stream velocities, U_∞ , from 15 m/s to 90 m/s. The corresponding Reynolds numbers (based on the *mac*) at $U_\infty = 90$ m/s were 2.0×10^6 and 2.2×10^6 for the 55° diamond wing and for the 65° delta wing, respectively. Flow visualization with laser-sheet smoke or oil flow and PIV measurements were also conducted in the experiments.

The third group (G3) is a family of delta wings with different sweep angles, thickness, leading- and trailing-edge bevel and with or without centerbody. The leading edge sweep ranged from 55° to 75°. In order to investigate the effect of the size of the leading-edge bevel

relative to the thickness of the boundary layer, a model with an enlarged leading-edge bevel (Fig. 4) was also tested in the IAR 38cm x 50cm water tunnel. All experiments were conducted at $U_\infty = 13.5$ cm/s corresponding to a Reynolds number of 1.2×10^5 per meter. Dye was injected through two 0.2 mm. diameter ports located at 5% c_0 and half local semi-span from the centerline on the windward side of the model. The flow was recorded by means of two CCD video cameras that provide a top and side views of the vortices. Part of these models had a five-component balance installed in the centerbody to measure the loads.

2.2 Test Matrix

The experimental envelope is briefly shown in the following table. A total of more than 1000 wind tunnel and water tunnel runs have been conducted between 2002 and 2003.

Model	Group 1	Group 2	Group 3
Facility	Wind tunnel	Wind tunnel	Water tunnel
α (deg.)	0~34	0~46, $\Delta\alpha=1$	0~50
ϕ (deg.)	0, 5, 7.5	-4, 0, 4, 180	0
U	15~90 m/s	15~90 m/s	13.5 cm/s
Re_{mac}	$0.38 \sim 2.2 \times 10^6$	$0.5 \sim 2.85 \times 10^6$	$1.2 \times 10^5/m$
Meas.	PSP Pressure taps Air loads Flow vis.	PSP Pressure taps Air loads Flow vis.	Air loads Flow vis.

2.3 Pressure Sensitive Paint technique (PSP)

Unlike the pressure orifices, the PSP provides the needed information over the whole model surface with a typical spatial resolution of one point every 0.5 to 1.5 mm², depending on the camera resolution and the optical arrangement [2]. The arrangement of the current PSP tests is shown in Fig. 5.

In the current experiments the material used in the PSP was a single layer of commercial paint called Unifib. The components of the paint (luminophore: PtFPP, polymer: FIB and light-scattering particles: TiO₂) were applied directly on the cleaned model. The illumination was provided by air-cooled green Halogen lamps filtered with a bandpass green colour

filter. The emission was collected with a 12-bit Photometrics CCD camera (CH 250) equipped with a 1024x1024 pixels cooled down to -30°C to minimize dark current. Melles Griot 650FS40 filter interference was mounted in front of the camera lens to cut off the excitation light.

In order to minimize the amount of noise, an average of 32 to 64 images was performed depending on the run condition. Before or after the wind-on images (I), reference images (I_{ref}) were acquired systematically at the same angles of attack without wind. The intensity ratio (I_{ref}/I) was required to cancel the illumination variation across the model and the paint non-uniformities in thickness or concentration.

The PSP response to pressure and temperature was obtained from laboratory calibration, so-called the *a priori* calibration.

In order to compare PSP data and the pressure tap data at the same locations, a relationship between the intensity image and the 3-D physical model coordinates was needed to account for the actual geometry (leading edge or fuselage curvature) and the camera perspective. This transformation, called the image registration, was performed using AFIX2 software developed by Y. Le Sant [3] at ONERA.

The image registration also allowed the alignment of the PSP images (reference and wind-on) in case of model motion during the test. In such a case, the CCD flat field correction was required in order to remove the effect of the camera lens and the variability of the CCD pixel-to-pixel response. After the dark image subtraction and the flat field correction, the images were aligned and the intensity ratio can then be performed. The intensity was finally converted to pressure by two different methods: the *in situ* and the *a priori* calibrations.

The *in situ* calibration consists of using the discrete pressure measurements on the model to correlate pressure and intensity ratio. The method is effective when pressure orifices adequately placed on the model are available, as in the case of the 65° delta wing.

For the 55° delta wing, only three pressure orifices were located on the wing centerbody, and the *in situ* calibration was no longer possible. In this case, the *a priori* calibration was applied assuming a uniform model temperature for every image. A single pressure orifice, located at 60% of the wing chord and on the wing centreline, was used to assess this model temperature using the *a priori* calibration, the local intensity ratio extracted at the orifice location and the pressure measurement.

2.4 Experimental Results

Significant were discovered in these experiments, only a few of which are presented here. Detailed information and more data can be found in Ref. [4].

The balance measurements show that there exist at least two critical states (discontinuity), corresponding to where the vortex breakdown location is at the trailing edge and at the apex, $x_{\text{VB}}=1$ and $x_{\text{VB}}=0$. As an example, Fig. 6 shows the normal force and pitching moment of the 55° delta wing with the sharp symmetrical bevel on both sides (Model G1-3C). The angle of attack at which the vortex breakdown is located at $x_{\text{VB}}=1$ and at $x_{\text{VB}}=0$ is also marked. It can be observed that two discontinuities exist, at $x_{\text{VB}}=1$ and $x_{\text{VB}}=0$. The second one at $x_{\text{VB}}=0$, where the vortex breaks down in the vicinity of the apex, exhibits a more severe discontinuity compared with the first one. Moreover, the angle of attack, at which the discontinuity appears, is more affected by the free stream velocity.

It was found that the leading-edge shape has a remarkable effect on the air loads and the discontinuities. Fig. 7 shows the measured normal force on different leading-edge shapes and centerbody setting. It appears that the model with the rounded leading-edge (Model G1-1A) is the last to reach the second discontinuity while the wing with a flat leeward side (G1-1D), but no centerbody (G1-1F), reaches the second discontinuity first as shown in Fig. 7. Moreover, the model with a large-radius leading-edge and centerbody could delay the secondary discontinuity by 4° in α and could

increase the maximum normal force by more than 10% (compare Fig. 7a with Fig. 7d). The water tunnel experimental results also confirm that if the bevel on the leeward side is large enough it will delay the vortex breakdown.

Compared with the effect of leading-edge shape, it seems that the centerbody causes less effect on the air loads as shown in Fig. 7, where the air loads with and without centerbody (G1-1D and G1-1F) are compared. Without the centerbody (G1-1F) the maximum normal force coefficient occurs at $\alpha=26^\circ\sim 28^\circ$ while with the centerbody the maximum force coefficient occurs at $\alpha=28^\circ\sim 29^\circ$.

Examples of measurements from the pressure orifices, with and without the centerbody (G2-3E and G2-3A), are shown in Fig. 8 for different angles of attack ($\alpha=22^\circ$ and 27°) and different chordwise locations ($x/c=0.4, 0.6$ and 0.75). The centerbody edge is at $y/s \approx 0.3, 0.22$ and 0.18 for $x/c = 0.4, 0.6$ and 0.75 respectively. There is a slight difference between with and without centerbody. At $x/c=0.4$ the pressure peak on G2-3E is slight lower than that of without centerbody (G2-3A). While at $x/c=0.75$ the pressure peak on 3E is slight higher than that of G2-3A. In addition, there is a little pressure bump in the centerbody area on G2-3E. It is noticed from Fig. 8 that only at higher angles of attack the centerbody causes more suction in the vicinity of the nose area. In general, no global effect is observed when the centerbody exists.

The information provided by PSP is particularly useful for the investigation in the vicinity of the leading-edge as other techniques, such as pressure orifices, are difficult to install there. Moreover, PSP measurements can provide global information which is particularly useful for CFD validation where the results need to be assessed everywhere on the model.

Validation tests have been firstly performed by the comparisons between the PSP measurements and those of the pressure taps. A typical comparison is shown in Fig. 9, which confirms that the present PSP results are reliable.

The general views of the PSP results on the 55° delta wing (G1) and the 65° wing (G2) with different leading-edge shapes and centerbody settings are shown in Fig. 10 and Fig. 11. For the sharp leading-edge, the leading-edge vortex starts right at the apex. While for the round leading-edge, the leading-edge vortex forms at almost 8% downstream of the apex. Moreover, the primary vortex or the main suction over the rounded leading-edge wing is more outboard compared with the sharp leading-edge delta wing. Furthermore, the secondary vortex is much weaker over the rounded leading-edge wing compared with the sharp leading-edge delta wing.

In order to fully understand these features, sectional views of the pressures in different directions were plotted taken from PSP results. Some examples of these sectional views normal to the chord wise direction are shown in Fig. 12 and Fig. 13 for the 55° diamond wing (G1-1A) and the 55° delta wing (G1-2A), respectively. Fig. 12a shows that the flow on the rounded leading-edge remains mainly attached up to 7% of the root chord length compared with the sharp leading-edge (Fig. 12b) where the vortex is already formed at 7% of the root chord. The suction peak on the rounded leading-edge reaches 6.5 while the maximum suction on the sharp leading-edge is only 4.8. Similar features can be observed by comparing Fig. 13a and Fig. 13b for the 55° delta wing with rounded or sharp leading-edge, respectively. This difference remains downstream of the vortex breakdown. Although at downstream of vortex breakdown the suction caused by the spiral flow is weaker than the concentrated vortex when compared Fig. 12c with Fig. 12d or Fig. 13c with 13d. The suction on the rounded leading-edge wing is still higher than that of the sharp leading-edge wing at downstream locations, implying that the vortex strength on the rounded leading-edge is still stronger than on the sharp leading-edge even downstream of the vortex breakdown. These results show that not only the location of the separation line on the rounded leading-edge is different from that of the sharp leading-edge, but also the vorticity

flux shedding from the boundary layer separation may be different from different leading-edge shapes. These observations should prove to be useful for vortex control and related aerodynamic performance. The vorticity within the boundary layer in the neighborhood of a separation line has an abrupt turning: from normal to the leading edge before separation, to the stream-wise direction after separation. Thus, the local shape of the leading-edge may have important effects on this separation process. This feature could be explored in the future by micro sensors and actuators along the leading-edge to gain extra control power.

The comparisons of section views between with and without centerbody are shown in Fig. 14 for the 65° delta wing model where the Model G2-3A is no centerbody and the Model G2-3E is with centerbody. Two sections are chosen for comparison i.e., $x/c=0.4$ and 0.6 . In general those comparisons agree with that of pressure orifice's measurements and no global effect of the centerbody is found.

3 Computational Approaches

The inviscid vortex flows over the 55° (model G1) and the 65° (model G2) wings were simulated using unstructured tetrahedral grids and an in-house Euler flow solver, FJ3SOLV. Only sharp-edged models of the wings were considered and medium size meshes were employed. The effects of the centerbody were investigated for one flow condition for each wing. N. Chaderjian [5] at NASA Ames and S. Pirzadeh [6] at NASA LaRC have obtained numerical results for the 65° delta wing model (G2) with different grid generation methods and flow solvers. Pirzadeh also conducted comparison studies between sharp, medium and large-radius leading-edges for the NASA LaRC 65° delta wing model. However, the effects of the centerbody on the vortex behavior remains to be solved. As mentioned by Pirzadeh [6], Euler solutions are capable of providing accurate predictions of vortex behavior on sharp leading-edge surfaces although the solutions may be problem dependent even for cases with

sharp leading edges. In addition, the difference in comparison studies about vortex behavior between with and without the centerbody, may be more reliable than the absolute value itself. Thus an Euler flow solver was used at IAR to study the effect of the centerbody on the vortex over sharp leading-edge delta wings.

3.1 Computational Grid

Since the wind tunnel model was tested under no sideslip ($\beta=0$) conditions, the flow was assumed symmetrical and only half of the wing was modeled in the computations to facilitate quicker CFD analyses. The unstructured tetrahedral meshes were generated using the Octree based Tetra module of ICEM CFD. The respective mesh sizes used for the different configurations of the two wings are summarized in the table below, where G1-1A and G2-3A refer to the wings without centerbody and G2-1C and G2-3E refer to the wings with centerbody. Surface grids of the model with centerbody models are shown in Figs. 15 and 18 for the 55° (G1-1C) and 65° (G2-3A) wings respectively.

Wing	Model	Mesh size	
		Grid Cells	Grid Points
55° diamond	G1-1A	344,000	66,000
	G1-1C	376,000	74,000
65° delta	G2-3A	450,000	87,000
	G2-3E	500,000	100,000

3.2 Flow Solver

The CFD solutions were obtained using a 3D unstructured grid Euler solver, FJ3SOLV, developed at IAR [7]. FJ3SOLV is a cell-centered code based on the finite volume formulation. The convective fluxes are discretized using Jameson's central difference scheme [8] where second and fourth order dissipation terms are added explicitly for stability. Time integration to steady state is achieved by means of an explicit 4-stage multi-step scheme and convergence is accelerated using a combination of local time stepping,

implicit residual smoothing, and enthalpy damping techniques.

Boundary conditions are imposed using fictitious cells outside the boundaries. Appropriate flow properties are set in these cells to satisfy the slip conditions on the solid boundaries, where the normal velocity is set to zero. At the far-field boundaries a characteristic approach based on Riemann invariants subject to one-dimensional analysis is used.

3.3 Numerical Results

The numerical results on the sharp-edged wings with and without centerbody are shown in Figs. 16 and 17 for the 55° diamond wing (model G1) and in Figs. 19 and 20 for the 65° delta wing (model G2). The respective free stream flow conditions considered in the CFD simulations are $M_\infty=0.18$, $\alpha=15^\circ$ for the G1 wing model and $M_\infty=0.17$, $\alpha=21^\circ$ for the G2 wing model. Figs. 16 and 19 illustrate the comparisons of global pressure distributions between with (G1-1A and G2-3A) and without (G1-1C and G2-3E) centerbody configurations. In general, there are no global differences in these comparisons for both wing models. The surface pressure along $x/c=0.4$, 0.6 and 0.75 are depicted in Figs. 17 and 20 for the G1 and the G2 models, respectively. There is only a slight difference between the two plots in Figs. 17 and 20. The vortex core location at $x/c=0.4$ is a little outboard with the centerbody than that without the centerbody. Moreover, it appears that the wing without the centerbody has slightly more suction in the forward portion and less suction in the aft portion as seen in Figs. 17a and 20a and Figs. 17c and 20c. There is little bump in the pressure distribution at $y/s \approx 0.3$, $x/c=0.4$ and $y/s=0.22$, $x/c=0.6$ (Fig. 20a and Fig. 20b). A similar phenomenon was observed in the PSP experiments as shown in Fig. 18. The above coordinates are that the centerbody edge location. The local flow acceleration on the centerbody shoulder may cause this local suction bump. Nevertheless, the comparisons show that centerbody may not cause global effects on the pressure distribution at the present conditions.

Pirzadeh recently has conducted an inviscid adapted Euler calculation and a viscous unadapted NS calculation on the same 65° delta wing geometry at $M_\infty=0.29$ and $\alpha=30^\circ$. Fig. 18 shows some of the results. Although the Mach number and angle of attack are different from present studies, the results have similar trends. It confirms that present numerical studies about the difference between with and without centerbody are helpful although more work needs to be done in the future.

4 Conclusions

- Balance measurements show two discontinuities exist at $x_{VB}=1$ and $x_{VB}=0$.
- The second one is more severe and is a function of speed and leading-edge shape.
- Rounded leading-edges could delay the second discontinuity by 4° in AOA and increase normal force by 10%.
- PSP results reveal that the suction peak near the rounded leading-edge in the forward portion is much larger than with the sharp leading-edge.
- PSP results show that the vortex formation and breakdown are delayed by rounded leading-edge.
- Present CFD results agree with experimental results.
- Both experimental and CFD results indicate the centerbody does not have any global effect.
- The results confirm that the present technologies can be applied to further studies to improve the performance of future UCAVs and combat vehicles.

References

- [1] Huang, X. Z. Comprehensive Experimental Studies on Vortex Dynamics over Military Wing Configurations in IAR. RTO Rep-084, Chapter 5, 2004.
- [2] Mébarki, Y., Cooper, K. and Reichert, T. M., "Automotive Testing Using Pressure-Sensitive Paint. Journal of Visualization, Vol 6, N 4, 2003.

- [3] Le Sant Y., Bouvier F. and Mérianne M.C. Mesures de la Pression Pariétale à l'Aide de Peintures Sensibles à la Pression. 9th FluVisu Conférence, Rouen, 2001.
- [4] Huang, X.Z. Progress in Experimental Studies on Leading-Edge Vortex Dynamics and Maneuvering Aerodynamics. IAR Report. To be published in 2004.
- [5] Chaderjian, N. M. and Schiff, L. B. Numerical Simulation of forced and Free-to-Roll Delta-Wing Motions. J. Aircraft Vol. 33, No. 1 Pages 93-99, 1996.
- [6] Pirzadeh, S. Z. CFD Prediction of Vertical Flows on Delta Wings Using an Adaptive Unstructured Grid Method," RTO AVT-80, "Vortex Breakdown over Slender Wings" Manchester, UK, 8-11 October 2001.
- [7] Fortin, F., Benmeddour, A. and Jones, D. J. Application of the Canadian Code to the F/A-18C JDAM Separation. AIAA Paper 99-0127, January 1999.
- [8] Jameson, A., Schmidt, W. and Turkel, E. Numerical Solution of the Euler Equations by Finite Volume Methods using Runge-Kutta Stepping Schemes. AIAA 81-1259.

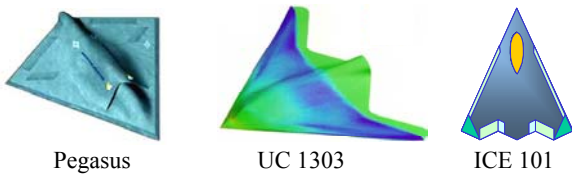


Fig. 1 Samples of UCAVs in development

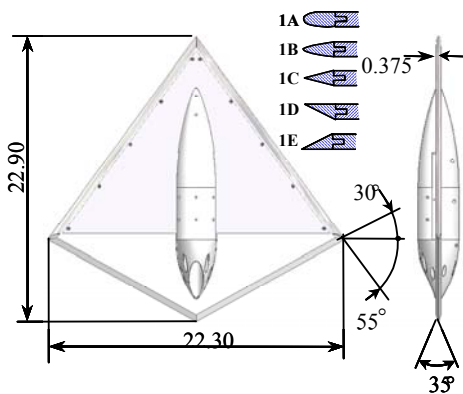


Fig. 2a 55° diamond wing model (G1-1)

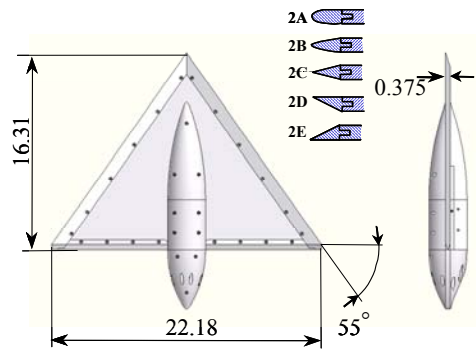


Fig. 2b 55° delta wing model (G1-2)

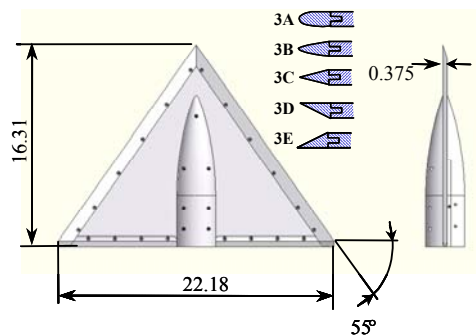


Fig. 2c 55° delta wing model (G1-3)

Fig. 2 55° diamond and delta wing models (G1)

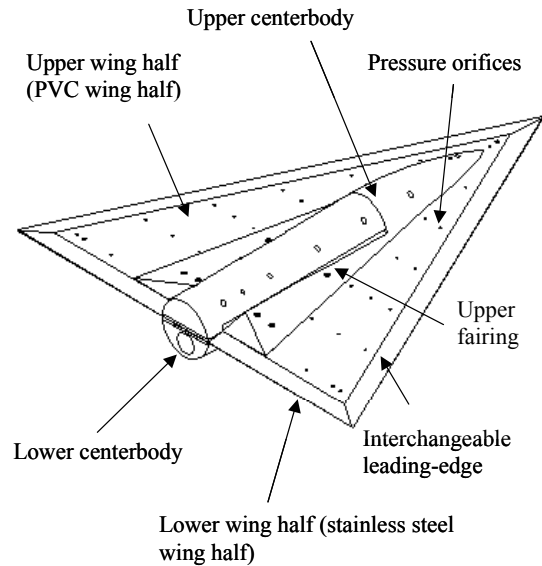


Fig. 3a Combinations of 65° delta wing model (G2)

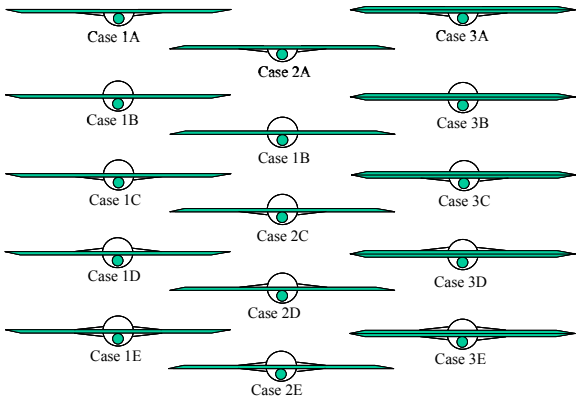


Fig. 3b Available model combinations (G2)

Fig. 3 65° delta wing models (G2)

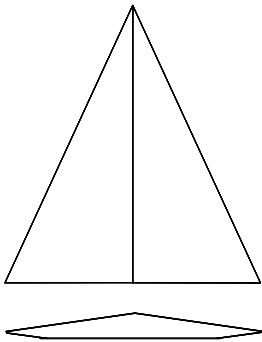


Fig. 4 Large bevel water tunnel delta wing model

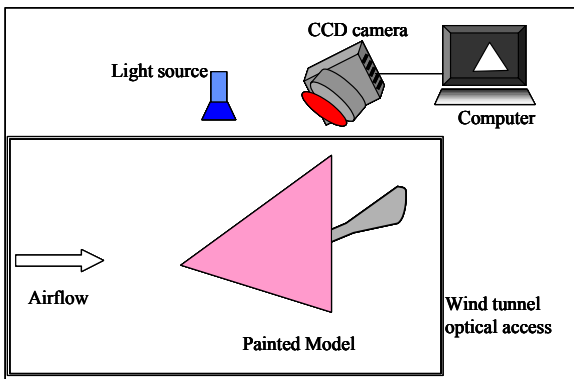


Fig. 5 PSP set-up

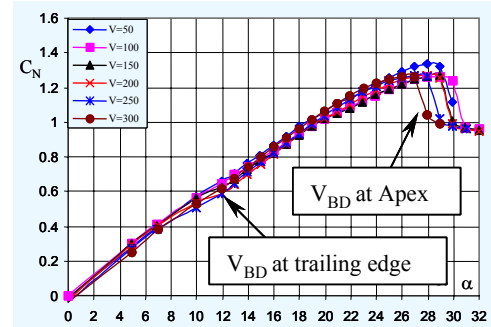


Fig. 6a Normal force discontinuities

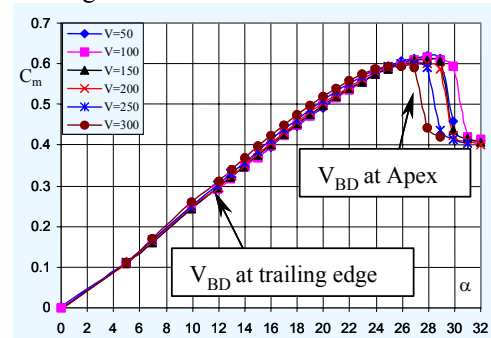


Fig. 6b pitching moment discontinuities

Fig. 6 Discontinuities caused by the leading-edge vortex breakdown (Model G1, 3C symmetrical bevel)

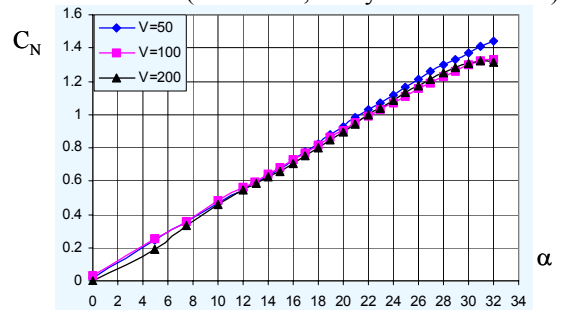


Fig. 7a Model G1, 1A (large-radius leading-edge)

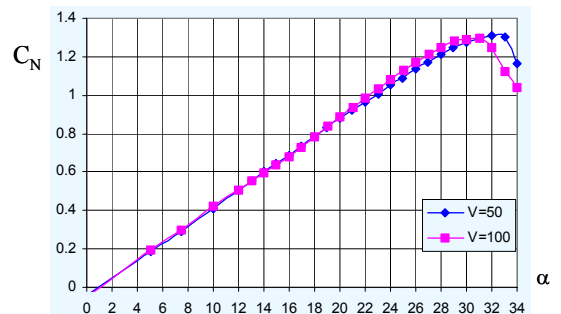


Fig. 7b Model G1, 1E (bevel on upper side)

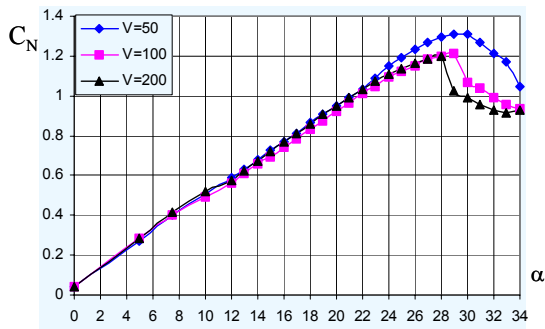


Fig. 7c Model G1, 1D (flat upper side)

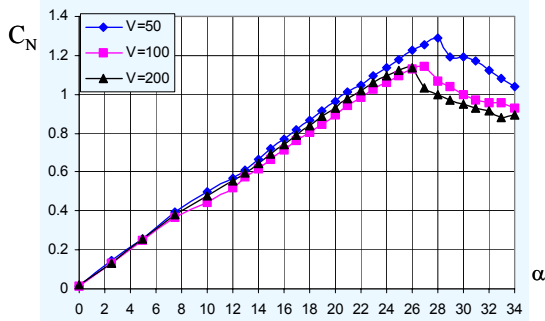


Fig. 7d Model G1, 1F
(flat upper side, no center body)

Fig. 7 Effect of the leading-edge shape and centerbody on the normal force discontinuity

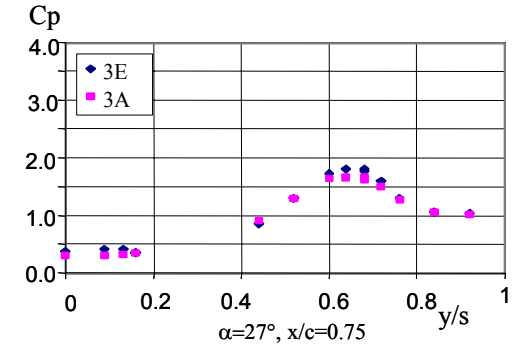
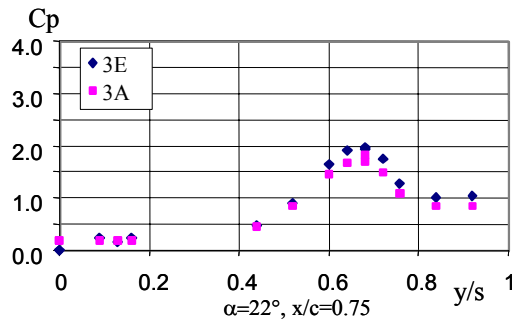
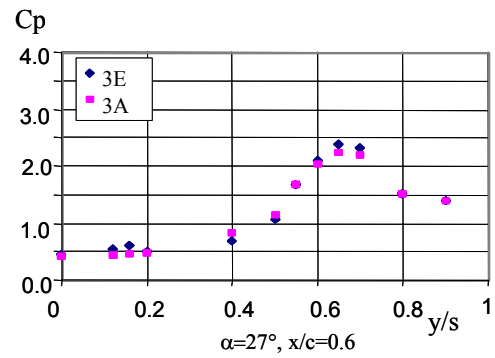
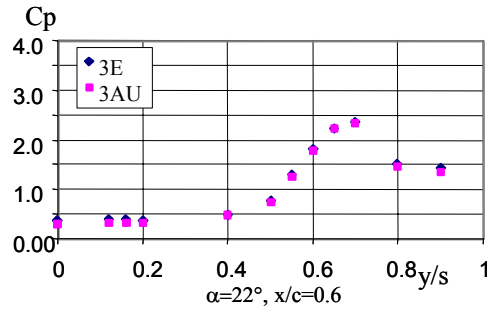
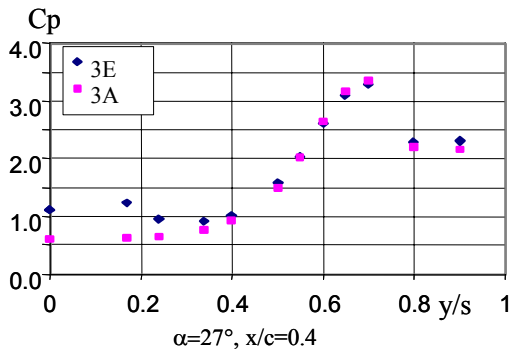
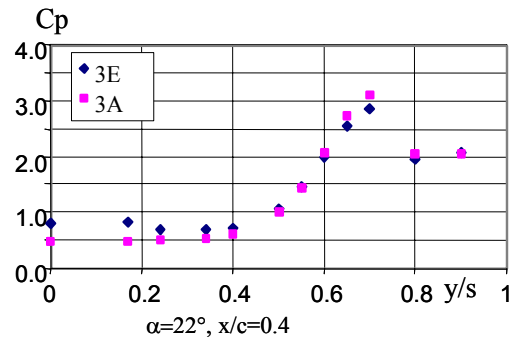


Fig. 8 Centerbody effect on pressure distributions at different locations, $U=60\text{m/s}$ (3E with centerbody; 3A without centerbody)

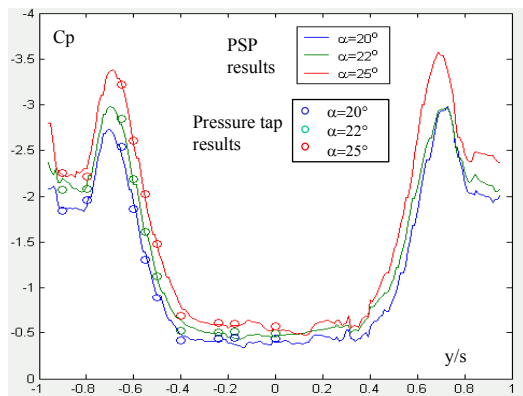


Fig. 9 Comparisons between PSP and pressure taps measurements, U=60 m/s

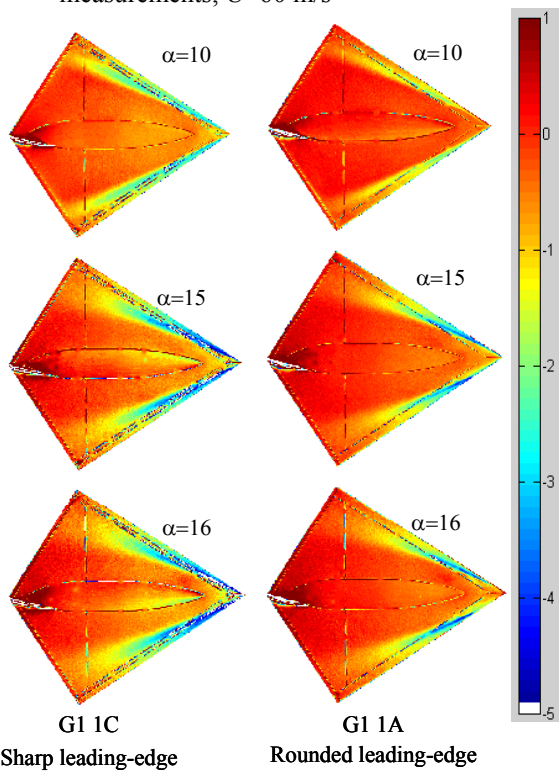


Fig. 10 General views of PSP results on Model G1 with different leading-edge shapes, U=60 m/s

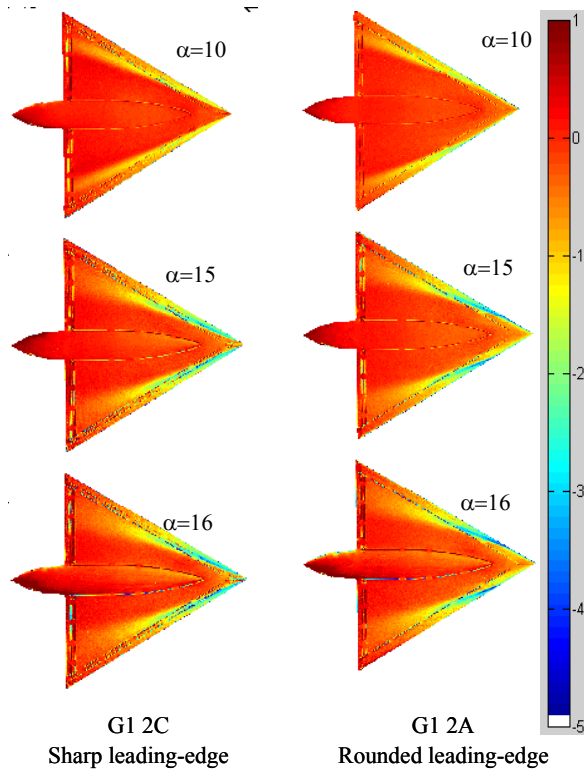


Fig. 10 (cont.) General views of PSP results on Model G1 with different leading-edge shapes, U=60 m/s

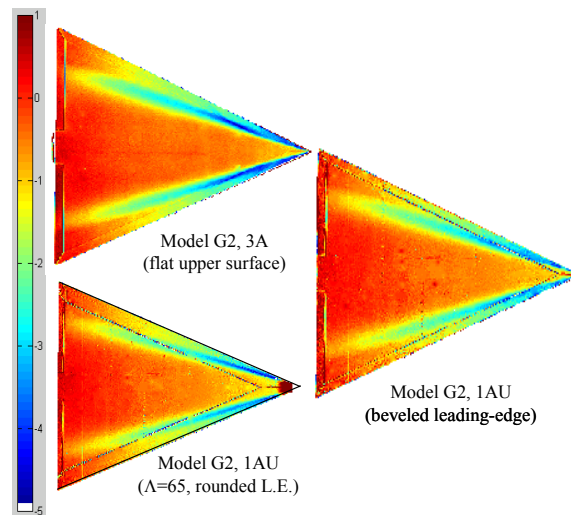


Fig. 11a different leading-edge shapes

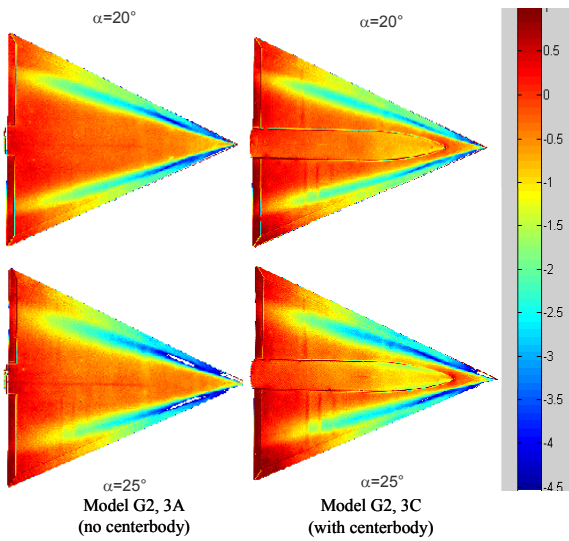


Fig. 11b with/without centerbody

Fig. 11 General views of PSP results on Model G2 with different combinations, $U=60$ m/s

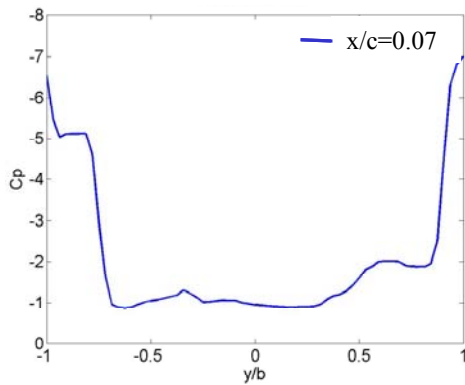


Fig. 12a Model G1 1A, large radius leading-edge

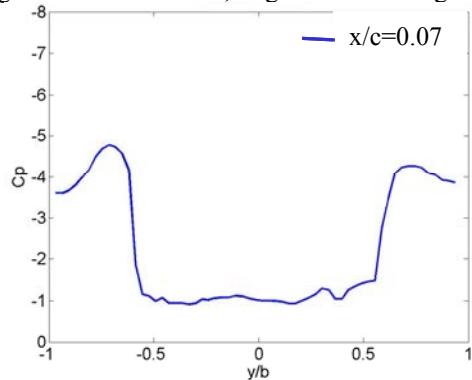


Fig. 12b Model G1 1C, sharp leading-edge

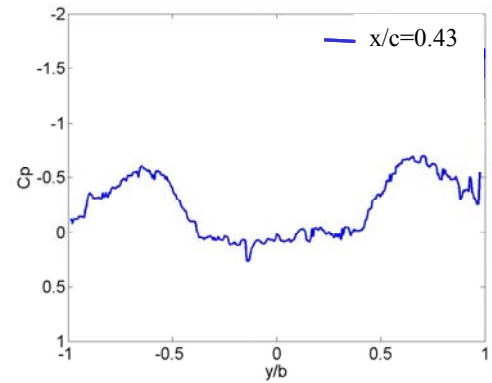


Fig. 12c Model G1 1A, large radius leading-edge

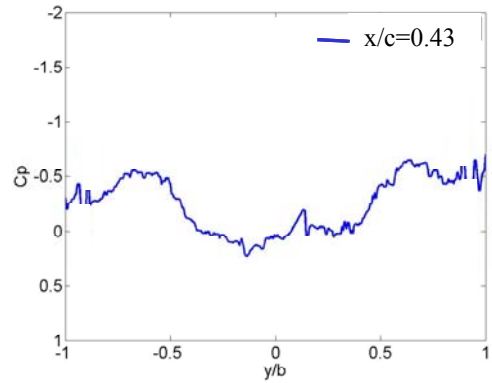


Fig. 12d Model G1 1C, sharp leading-edge

Fig. 12 Leading-edge shape effect on PSP results ($U=60$ m/s, $\alpha=21^\circ$)

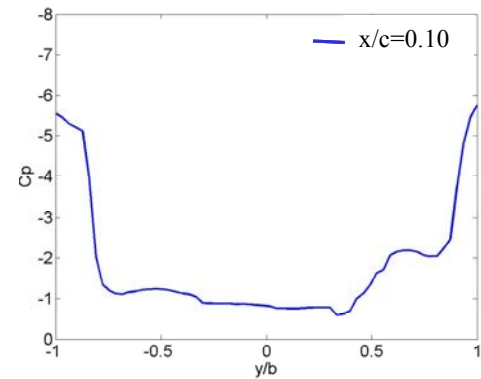


Fig. 13a Model G1 2A, large radius leading-edge

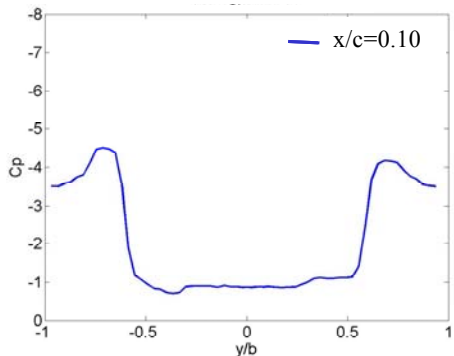


Fig. 13b Model G1 2C, sharp leading-edge

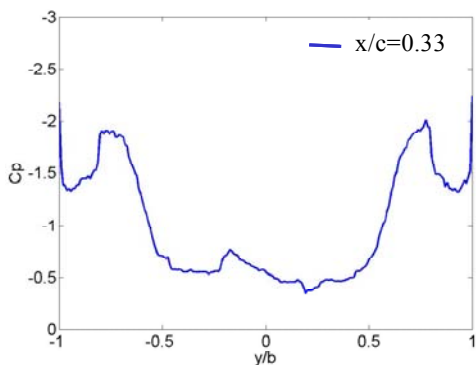


Fig. 13c Model G1 2A, large radius leading-edge

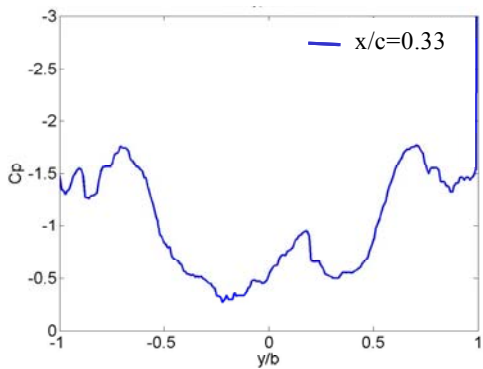


Fig. 13d Model G1 2C, sharp leading-edge

Fig. 13 Leading-edge shape effect on PSP results
($U=60$ m/s, $\alpha=21^\circ$)

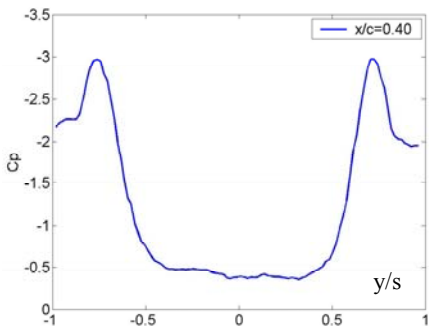


Fig. 14a Model 3A (no centerbody)

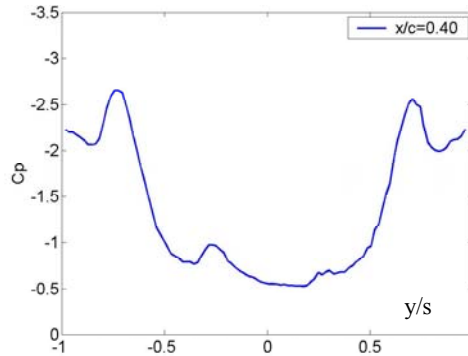


Fig. 14b Model 3E with centerbody

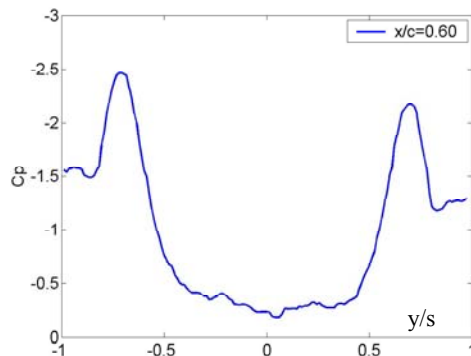


Fig. 14c Model 3A no centerbody

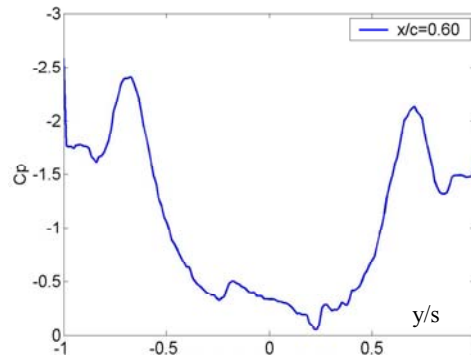


Fig. 14d Model 3E with centerbody

Fig. 14 Comparisons of PSP results between with and without centerbody ($U=60$ m/s, $\alpha=21^\circ$)

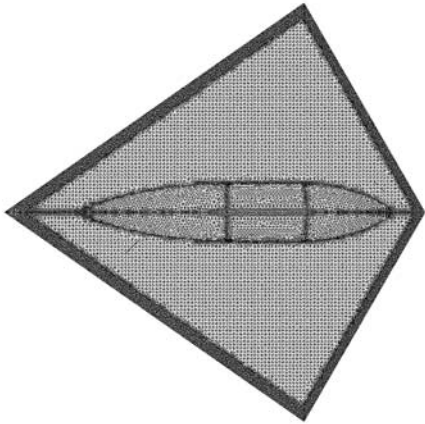


Fig. 15 Surface grid with centerbody (Model G1-1C)

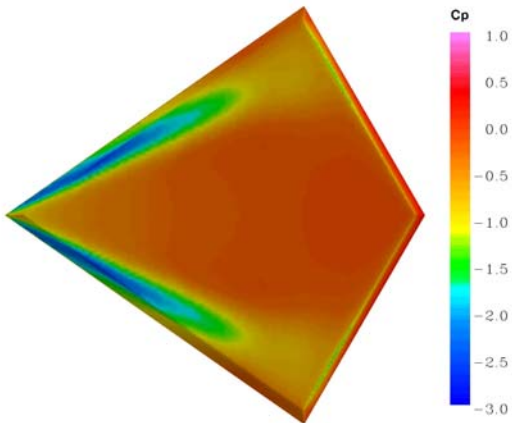


Fig 16a Surface pressure (no centerbody, G1-1A)

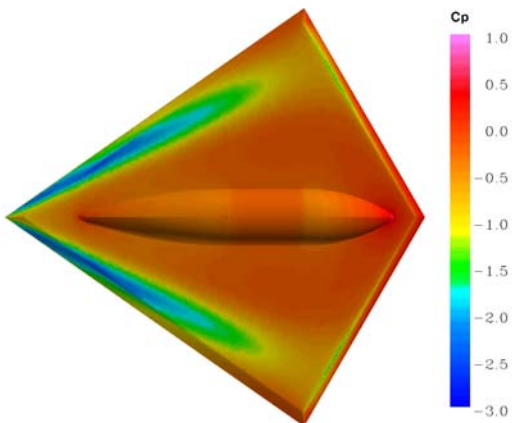


Fig 16b Surface pressure (with centerbody, G1-1C)

Fig. 16 Comparison of surface pressure between with and without centerbody (Model G1, $M=0.18$, $\alpha=15^\circ$)

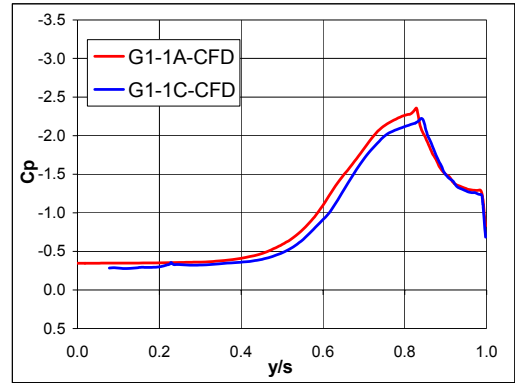


Fig. 17a $x/c=0.4$

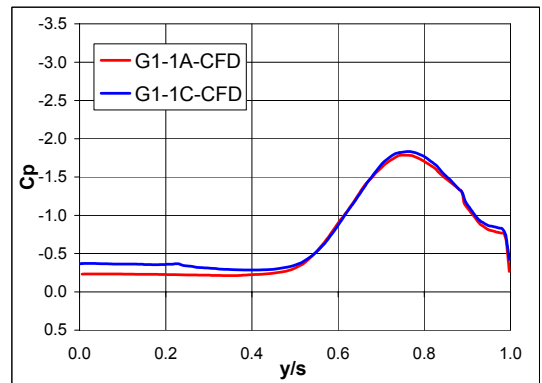


Fig. 17b $x/c=0.6$

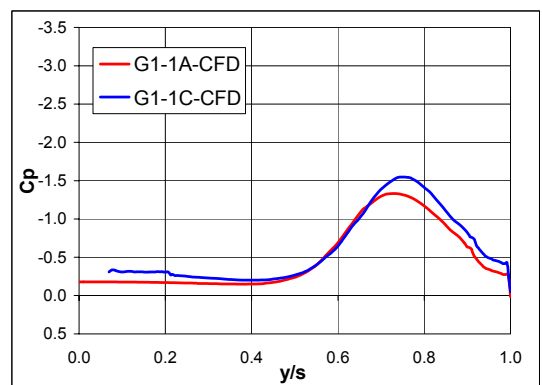


Fig. 17c $x/c=0.75$

Fig. 17 Comparisons of pressure distributions between with/without centerbody at different chordwise locations ($M=0.18$, $\alpha=15^\circ$, NF no centerbody, 3E with centerbody)

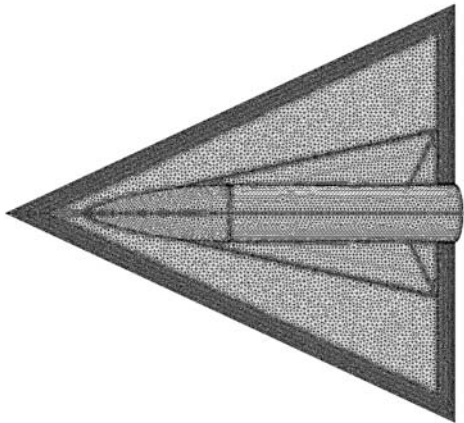


Fig. 18 Surface grid with centerbody (Model G2-3E)

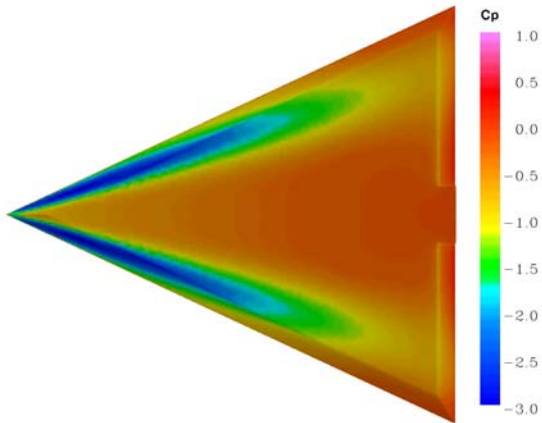


Fig 19a Surface pressure (no centerbody, G2-3A)

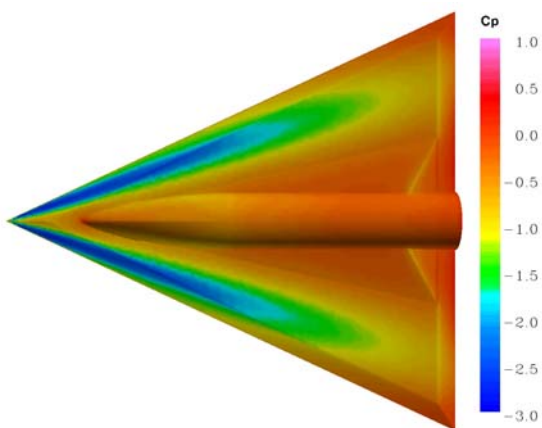


Fig 19b Surface pressure (with centerbody, G2-3E)

Fig. 19 Comparison of surface pressure between with and without centerbody (Model G2, $M=0.17$, $\alpha=21^\circ$)

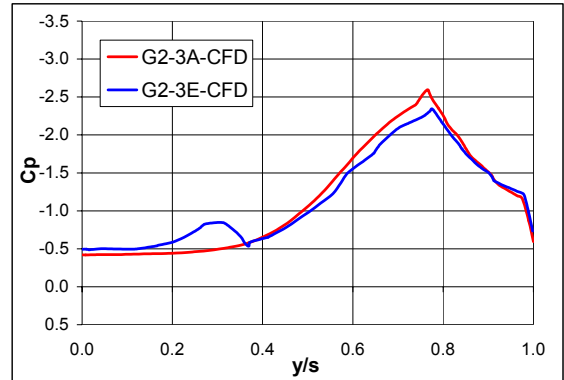


Fig. 20a $x/c=0.4$

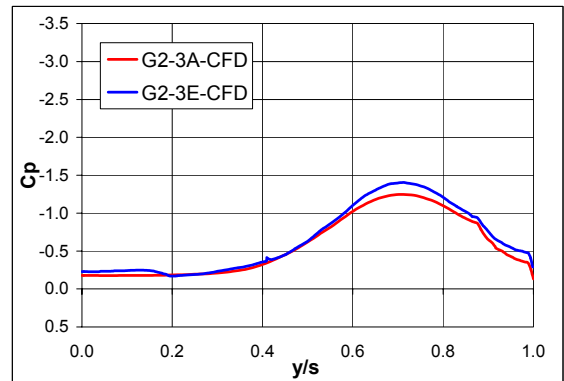


Fig. 20b $x/c=0.6$

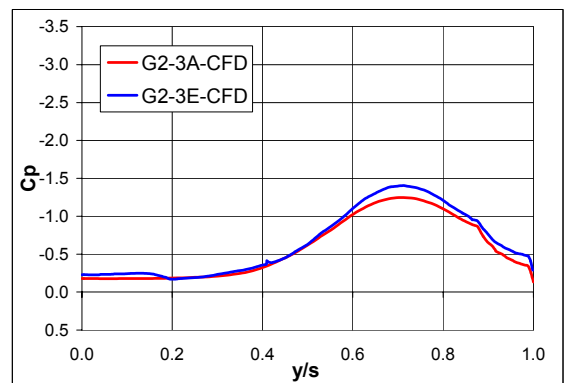


Fig. 20c $x/c=0.75$

Fig. 20 Comparisons of pressure distributions between with/without centerbody at different chordwise locations ($M=0.17$, $\alpha=21^\circ$, 3A no centerbody, 3E with centerbody)

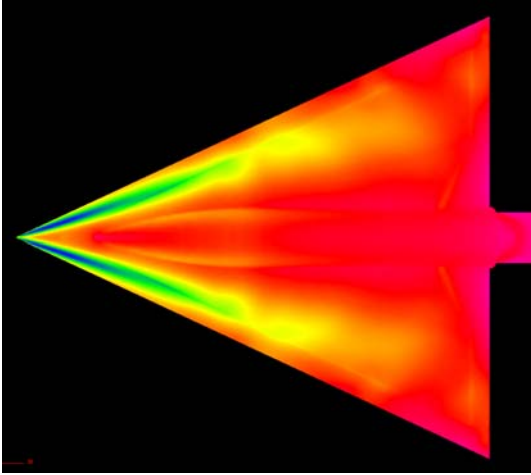


Fig. 21a Adapted Euler solution (Pirzadeh [6])

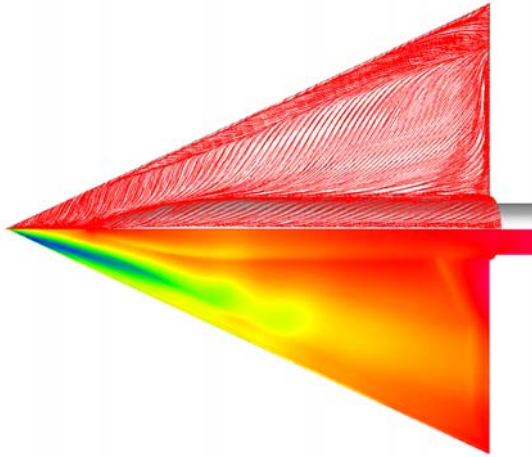


Fig. 21b Unadapted N-S solution

Fig. 21 Adapted Euler and unadapted N-S solutions for IAR 65° delta wing at $M=0.29$, $\alpha=30^\circ$ (Pirzadeh [6])